Böse, M., Horleston, A. C., Stähler, S. C., Deichmann, D., Giardini, D., Clinton, J., Lognonné, P., Ceylan, S., van Driel, M., Charalambous, C., Dahmen, N. L., Kawamura, T., Khan, A., Knapmeyer, M., Orhand-Mainsant, G., Scholz, J.-R., Euchner, F., & Banerdt, W. B. (2021). Magnitude Scales for Marsquakes Calibrated from InSight Data. *Bulletin of the Seismological Society of America*. Advance online publication. https://doi.org/10.1785/0120210045

Peer reviewed version

Link to published version (if available):
10.1785/0120210045

Magnitude Scales for Marsquakes Calibrated from InSight Data

Böse, M.*, S. Stähler, N. Deichmann, D. Giardini, J. Clinton, P. Lognonné, S. Ceylan, M. van Driel, C. Charalambous, N. Dahmen, A. Horleston, T. Kawamura, A. Khan, M. Knapmeyer, G. Orhand-Mainsant, J.-R. Scholz, F. Euchner, B.W. Banerdt

*Corresponding author: Maren Böse, maren.boese@sed.ethz.ch, Institute of Geophysics, ETH Zurich, Sonneggstrasse 5, 8092 Zurich, Switzerland

The authors acknowledge there are no conflicts of interest recorded.

ABSTRACT

In preparation for the NASA InSight (Interior exploration using Seismic Investigations, Geodesy and Heat Transport) Discovery Program mission, Böse *et al.* (2018) calibrated magnitude scales for marsquakes that incorporated the pre-launch knowledge on Mars' interior structure and the expected ambient and instrumental noise. Now, using data collected during the first two years after the successful deployment of the InSight very-broadband seismometer on the Martian surface, we revise these relations to account for the seismic and noise characteristics observed on Mars. The data collected so far (until October 12, 2020) includes 485 seismic event detections and suggest that (1) marsquakes are characterized by energy between ~0.1 and 10 Hz; (2) though first arriving P- and S-wave phases are regularly identified and assigned, both surface-waves and secondary phase arrivals are extremely challenging to identify; (3) the majority of identified events include a strong excitation of an unexpected 2.4 Hz ground resonance; and (4) so-called high-frequency events exist that are visible mainly as guided P_g/S_g wave trains. In view of these observations, we update our scaling relations for the spectral and body-wave magnitudes, $M_{W,\mathrm{spec}}^{\mathrm{Ma}}$, $m_{\mathrm{b}}^{\mathrm{Ma}}$ and $m_{\mathrm{b}S}^{\mathrm{Ma}}$, and introduce a new magnitude scale, $M_{2.4}^{\mathrm{Ma}}$, for high-frequency events. We use these scales to determine that the magnitudes of events in the current InSight v.5 catalog range between 1.1 and 3.7, with event-specific uncertainties σ_M ranging from 0.2 to 0.5. Due to the currently unclear interpretation of high-frequency events, magnitude estimates for these events primarily serve for a relative comparison.

INTRODUCTION

The NASA InSight (Interior exploration using Seismic Investigations, Geodesy and Heat Transport) Discovery Program mission successfully launched on May 5, 2018, from Vandenberg Air Force Base, California, and landed on Mars about six months later (Banerdt *et al.*, 2020). The deployment of the three-component ultra-sensitive very-broadband (VBB) seismometer (Lognonné *et al.*, 2019; 2020) was completed by the end of February 2019 (Giardini *et al.*, 2020). Since then, the Marsquake Service (MQS), as part of the InSight Science Team, routinely inspects manually the continuous 20 samples-per-second (sps) seismic data returned by InSight (Clinton *et al.*, 2018). Event data at higher sampling (100 sps) is recovered whenever possible. (The available bandwidth depends on multiple factors related to satellites around Mars that relay the data, as well as competing data volumes from other Martian missions and even other instruments operating on InSight.) Until October 12, 2020 (first Martian year of the InSight mission), MQS has identified 485 seismic events that have been interpreted as marsquakes (InSight Marsquake Service, 2021). All of these events are characterized by energy between ~0.1 - 10 Hz and have durations typically ranging from 5 - 30 minutes. A small number of events include energy of up to 35 Hz. Waveform amplitudes typically rise only slightly above the lowest background noise, and this lowest noise typically occurs only for a few hours per sol (a Martian sol is 24h 39.5' long). A detailed description of the event catalog and general characteristics of the data collected so far are given in Clinton *et al.* (2020), Giardini *et al.* (2020), and Ceylan *et al.* (2020); noise and event amplitudes are discussed in Charalambous *et al.* (2021).

The seismic events identified in the InSight MQS catalog fall into two families (Clinton *et al.*, 2020). A low-frequency family, which is similar to terrestrial earthquakes, comprises events with clearly defined P- and S-wave arrivals, even though they may have low signal-to-noise ratios (SNR). A second family of high-frequency events is characterized by long-duration wave trains, similar to guided Po/So waves in the oceanic crust (Kennett & Furumura, 2013). The MQS further divides the two events families into the following five classes:

- Low-frequency family:
  - *low-frequency* (*LF*) events have energy on all 3 components below 2.4 Hz;
  - *broadband* (*BB*) events have energy on 3 components, predominantly below 2.4 Hz, but

also including excitement at and possibly also above 2.4 Hz;

- High-frequency family:
  - *high-frequency* (*HF*) events have energy on 3 components, predominantly at 2.4 Hz and above;
  - *very high-frequency* (*VF*) events are a special case of *HF* events with energy on the horizontal components at higher frequencies being significantly larger than on the vertical;
  - *2.4Hz resonance* (*2.4Hz*) events have energy on 3 components, centered around 2.4 Hz (ambient) resonance with very limited excitation above or below (likely small amplitude *HF* events).

An additional class of signals, *super-high frequency* (*SF*) events, are also included in the MQS catalog. These events have an order of magnitude shorter durations than the other events and only include energy above 5 Hz. They are considered to be associated with a very local source (Dahmen *et al.*, 2021), but further research is needed to provide a stable interpretation of these signals. *SF* events are not considered further in this study.

The InSight catalog v.5 (until 2020/10/12; sol 668) holds a total of 279 seismic events with distance estimates of any kind (and an additional 206 events without distance estimates or of unclear origin), including 20 *LF* ($20^o \leq \Delta \leq 100^o$), 9 *BB* ($25^o < \Delta < 90^o$), 50 *HF* ($20^o < \Delta < 30^o$), 21 *VF* ($3^o < \Delta < 30^o$), and 179 *2.4Hz* ($6^o < \Delta < 40^o$) events (Table 1). The *2.4Hz* events are likely weak examples of *HF* events that would not be observable, but for the additional excitation of the 2.4 Hz subsurface resonance rising above the background noise (Clinton *et al.*, 2020). *VF* events are *HF* events with clear differences in energy between horizontal and vertical components and a rising displacement spectrum on the horizontal components. Following Giardini *et al.* (2020) and van Driel *et al.* (2021), our current understanding is that the seismic waveforms of events in the high-frequency (*HF*, *VF*, *2.4Hz*) family are dominated by guided crustal waves in a shallow layer. This could be a regional sediment layer, or in the most extreme case, the whole crust and lithosphere, as observed in the oceanic crust on Earth (Kennett & Furumura, 2013). The assumed propagation path of seismic waves in the two event families is illustrated in Figure 1.

The MQS assigns event quality according to the following conventions: (1) High-quality events ('A') show multiple clear and identifiable phases and clear polarisation (i.e. they can be located using the probabilistic approach of Böse *et al.*, 2016); (2) medium quality events ('B') show multiple clear and identifiable phases, but no polarisation (i.e. only their distance from the lander can be determined, but no absolute location); (3) low-quality events ('C') show no clear phases, but signals are clearly observed; and (4) suspicious events ('D') show only weakly observed signals or signals that may not be attributable to a seismic event. In addition to this quality scheme, all events are characterized by an SNR measurement (Giardini *et al.*, 2020; Charalambous *et al.*, 2021).

In the v.5 MQS catalog, distance estimates are available for all quality 'A' and 'B' events, and for the majority of quality 'C' and some quality 'D' events. A complete description of the approach is given in Clinton *et al.* (2020) and is summarized below. For low-frequency family events the methodology follows Böse *et al.* (2016). Using large sets of travel time tables derived from a priori velocity models, distances are computed using picks identified in either the time or spectral domain that are interpreted as P- and S- phases. This allowed to constrain 15 of the 43 low-frequency family events in distance. Further work using alignment of waveform envelopes allows these distances to be refined and additional events that do not have clear onsets to be assigned distances (see Giardini *et al.*, 2020). In this manner, 27 of the 43 (63%) low-frequency family events in the MQS catalog are assigned distances. In cases where there are differences between distances based on phase picks and alignments, the alignment-based distances are preferred. For events in the high-frequency family, picks are typically identified using a STA-LTA filter targeting the 2.4 Hz resonance. Two phase onsets are normally visible, that are interpreted as P_g and S_g. Since the propagation velocities of those are not known, we cannot confidently determine absolute distances. In order to provide an approximate distance, as well as a robust estimate of the relative distances within the high-frequency family, we assume that P_g propagates with v_p = 4 km/s and S_g with $v_s = v_p/\sqrt{3}$ = 2.3 km/s. For 249 of 441 (56%) high-frequency family events in the MQS catalog, P_g and S_g phases are both identified and we could assign distances this way.

Pre-Launch Magnitude Calibrations

Assigning event magnitudes is an important part of characterizing seismicity. In our pre-launch paper (Böse *et al.*, 2018) we had calibrated magnitude scales for marsquakes by simulating the seismic wave propagation through a set of hypothetical 1D Mars models, that incorporated the pre-mission knowledge on Mars interior structure (Smrekar *et al.*, 2019) and the assumed ambient and instrumental noise (Murdoch *et al.*, 2015; Mimoun *et al.*, 2017), using the spectral element solver AxiSEM (Nissen-Meyer *et al.*, 2014; van Driel *et al.*, 2017). Inspired by relations developed for Earth, we had defined six magnitude scales: local Mars magnitude, $M_{\mathrm{L}}^{\mathrm{Ma}}$; P- and S-wave magnitudes, $m_{\mathrm{b}}^{\mathrm{Ma}}$ and $m_{\mathrm{bS}}^{\mathrm{Ma}}$, at a period of 3 s; surface-wave magnitude, $M_{\mathrm{s}}^{\mathrm{Ma}}$; and spectral magnitudes, $M_{\mathrm{FB}}^{\mathrm{Ma}}$ and $M_{\mathrm{F}}^{\mathrm{Ma}}$. We had calibrated these scales relative to the seismic moment magnitude at $M_W = 5.5$ by correcting filtered phase or spectral amplitudes in the simulated waveforms for distance-dependent attenuation using

$$M_i^{\mathrm{Ma}} = log_{10}(A_i) + a_i\, log_{10}(\Delta) + c_i \qquad (1)$$

The superscript "Ma" stands for "Mars" (following BSSA accepted standard for planetary magnitude in accordance with IAU practice); a_i and c_i are scaling coefficients for the different magnitude types; A_i is a measure of amplitude that is also dependent on magnitude type – and can be the filtered peak displacement amplitude $[m]$ determined from the waveform time-series within a certain time-window, or the spectral amplitude $[m/\sqrt{Hz}]$ determined from the square-root of the long-period plateau of the power spectral density (PSD) of the displacement; Δ is the epicentral distance in degrees $[^o]$. For both the local and the surface-wave based magnitude scales, Böse *et al.* (2018) included an additional term for source depth. In a second regression, Böse *et al.* (2018) had calibrated the six scales with the known seismic moment, M_0, of the simulations across the entire magnitude range $1.0 \leq M_W \leq 7.0$ to obtain a conversion relation to moment magnitude M_W.

The InSight data collected so far suggest that (1) two families of marsquakes exist (low-frequency and high-frequency; see above), which need separate magnitude scales, (2) the frequency content of the more classic low-frequency events ranges from 0.1 to 1 Hz, the high-frequency events from

1.5 to up to 10 (and possibly larger) Hz, (3) though first arriving P- and S-wave phases are regularly identified and assigned, both surface-waves and secondary phase arrivals are extremely challenging to identify and cannot be used for regular analysis, and (4) many high-frequency events are primarily visible as an enhanced excitation of the natural 2.4 Hz ambient mode, which is believed to originate from the substructure below the lander (Ceylan *et al.*, 2020; Dahmen, Zenhäuser *et al.*, subm.). In view of these observations, we update our scaling relations (Böse *et al.*, 2018) for the body-wave magnitudes, $m_{\mathrm{b}}^{\mathrm{Ma}}$ and $m_{\mathrm{b}S}^{\mathrm{Ma}}$, and introduce a new magnitude scale, $M_{2.4}^{\mathrm{Ma}}$, specifically, for high-frequency events. The surface-wave magnitude, $M_{\mathrm{S}}^{\mathrm{Ma}}$, is not updated, given the lack of clear surface-wave observations (which is likely due to the small sizes of marsquakes detected so far; Clinton *et al.*, 2020), and as explained in the following section, we replace the spectral magnitude $M_{\mathrm{FB}}^{\mathrm{Ma}}$ introduced in Böse *et al.* (2018) by $M_{W,\mathrm{spec}}^{\mathrm{Ma}}$.

METHOD

Based on the data in the InSight v.5 event catalog (until 2020/10/12; InSight Marsquake Service, 2021) and formulations of Böse *et al.* (2018), we calibrate in this study four magnitude scales: spectral magnitude, $M_{W,\mathrm{spec}}^{\mathrm{Ma}}$ (computed over the full body-wave train), time-domain P- and S-body-wave magnitudes, $m_{\mathrm{b}}^{\mathrm{Ma}}$ and $m_{\mathrm{b}S}^{\mathrm{Ma}}$, and 2.4 Hz magnitude, $M_{2.4}^{\mathrm{Ma}}$. We will describe each scale in detail in the following subsections. The MQS tracks and internally catalogs the corresponding amplitudes (they are given in Table S1 in the Electronic Supplement of this article): spectral plateau amplitude, A_0, for low- and high-frequency events (excluding the majority of *VF* events that often have unclear A_0 and all *2.4Hz*); time domain body-wave amplitudes, A_P and A_S, at 0.2 - 0.5 Hz for low-frequency events (*LF*, *BB*); and 2.4 Hz spectral and time domain amplitudes, $A_{2.4,\mathrm{spec}}$and $A_{2.4,\mathrm{pick}}$, for high-frequency events (*HF*, *VF*, *2.4Hz*). Examples of each type are shown in Figure 2.

Unlike in Böse *et al.* (2018), we calibrate each magnitude directly against the moment magnitude, M_W, which is possible for the limited magnitude range (< 4) that we work in. We adopt the definition of moment magnitude, M_W, for Earth, which is based on the seismic moment, M_0 [in MKS units] (Hanks and Kanamori, 1979):

$$M_W = \frac{2}{3}\,(log_{10}(M_0) - 9.1) \tag{2a}$$

Assuming that the far-field displacement, $\boldsymbol{u}(\boldsymbol{x},\tau)$, due to the direct S-wave from the source to the receiver is a unipolar pulse and that M_0 is proportional to the area under this pulse, it follows (e.g. Aki & Richards, 1980)

$$M_0 = \frac{4\pi\rho {v_s}^3}{R_S^{\theta\phi} S_f} R \int_0^T \boldsymbol{u}(\boldsymbol{x},\tau)d\tau = c_0 R \Omega_0 \tag{2b}$$

with average radiation pattern $R_S^{\theta\phi}$, free-surface amplification S_f, hypocentral distance R, density ρ , shear-wave velocity v_s at the source, and spectral displacement amplitude-density $\Omega_0 = \int_0^T \boldsymbol{u}(\boldsymbol{x},\tau)d\tau$ at frequency 0. Inserting equation (2b) in (2a) gives

$$M_w = \frac{2}{3}(log_{10}\Omega_0 + 1.0\ log_{10}R + \ log_{10}c_0 - 9.1) \tag{2c}$$

To describe the spectral magnitude on Mars, we adopt in this study a more general form

$$M_{W,\mathrm{spec}}^{\mathrm{Ma}} = \frac{2}{3}(log_{10}A_0 + a_i\ log_{10}\Delta + \ c_i) \tag{3a}$$

where A_0 $[m/\sqrt{Hz}]$ is the square-root of the spectral amplitude extrapolated from the long-period plateau of the event power spectral density (PSD) displacement spectrum. As a consequence of the relation between amplitude spectral density and power spectral density, it is $\Omega_0 = A_0/\sqrt{T}$, where T is the length of the data window used in the computation of the PSD. We replaced in equation (3a) the hypocentral R $[m]$ by the epicentral distance Δ $[^o]$, assuming that the seismic ray paths have a curvature similar to the curvature of the Martian surface. In equation (3a), $log_{10}\left(\sqrt{T}\right)$ as

well as the logarithm of the conversion factor between meters and degrees are included in the additive coefficient c_i.

In this study, $M_{W,\mathrm{spec}}^{\mathrm{Ma}}$ is set as a reference for the calibration of the other magnitude scales for events with measurements of multiple amplitude types (Figure 3). This is because (1) we consider the $M_{W,\mathrm{spec}}^{\mathrm{Ma}}$ the most reliable measurement of the seismic moment, M_0, and thus M_W, because it is estimated from the extrapolated spectrum at long periods (20 - 100 s), thus mitigating the effect of attenuation; (2) due to the low SNR of many events, the picking of peak amplitudes in the time domain is less robust compared to the calculation of a spectrum of a long time window, considering the duration of these events generally range from 5 - 30 minutes (Figure 2); and (3) aside from the majority of *VF* and all *2.4Hz* resonance events, $M_{W,\mathrm{spec}}^{\mathrm{Ma}}$ can be determined for all low- and high-frequency events in the InSight MQS catalog (Table 1 & Figure 3).

In order to derive magnitude scales that approximate M_W and that can be applied to quantify the source sizes of all events in the InSight catalog regardless of their frequency content, we will start this work with an absolute calibration of $M_{W,\mathrm{spec}}^{\mathrm{Ma}}$ (strictly speaking of $M_{W,\mathrm{spec},LF}^{\mathrm{Ma}}$ for low-frequency and of $M_{W,\mathrm{spec},HF}^{\mathrm{Ma}}$ for high-frequency events) relative to M_W, based on synthetic data and theoretical considerations, respectively. Then, in the next step, we use the low-frequency events (*LF*, *BB*) in the InSight catalog to calibrate body-wave magnitudes, $m_{\mathrm{b}}^{\mathrm{Ma}}$ and $m_{\mathrm{bS}}^{\mathrm{Ma}}$, relative to $M_{W,\mathrm{spec},LF}^{\mathrm{Ma}}$, and the high-frequency events (*HF*) to calibrate the 2.4 Hz magnitude, $M_{2.4}^{\mathrm{Ma}}$, relative to $M_{W,\mathrm{spec},HF}^{\mathrm{Ma}}$ (Figure 3). The resulting $M_{2.4}^{\mathrm{Ma}}$ scale can be applied also to the *VF* and *2.4Hz* events to obtain magnitude estimates that are comparable to the other events in the InSight catalog, and hence ensure that every marsquake with an assigned distance also has a magnitude.

Our magnitude calibration is done by regressing the InSight data to determine the coefficients a_i and c_i in equation (1). This equation predicts a power decay of seismic amplitudes, i.e. a constant a_i factor for all magnitudes and distances. This assumption, however, is valid only for events outside the low (S-wave) amplitude-zone between 35° and 60° (e.g. Giardini *et al.*, 2020). Therefore, we use only S-wave amplitudes for events outside this zone for magnitude calibration

of m_{bS}^{Ma}.

Absolute Calibration of Spectral Magnitude $M_{W,spec}^{Ma}$

We start with an absolute calibration of spectral magnitude $M_{W,spec}^{Ma}$(strictly speaking of $M_{W,spec,LF}^{Ma}$ and $M_{W,spec,HF}^{Ma}$) with M_W adopting the functional form in equation (3a). The spectral magnitude can be computed for all low- and high-frequency events, excluding *VFs* that have unclear A_0 and all *2.4Hz* events, in the InSight event catalog (Figure 3) using their spectral amplitude, A_0 (Figure 2). The corresponding spectra are computed from the instrument-corrected displacement waveforms that have been rotated into ZNE (up-down, north-south, east-west) components, from which the linear trend has been removed. We apply Welch's power spectral density (PSD) method to 25.6 s long Hanning-windowed time segments with 50% overlap and with zero-padding to 4096 samples (102.4 s), and then compute the square-root of the resulting spectrum. From the amplitude and slope between 0.1 and 0.8 Hz, the low-frequency plateau of the spectrum is extrapolated.

To determine the spectral amplitude, A_0 $[m/\sqrt{Hz}]$, we fit the following function to the spectra (vertical component)

$$A(f) = A_0\, A_{src}(f)\, A_{att}(f) \tag{4a}$$

which combines a simple source spectrum (Brune, 1970)

$$A_{src}(f) = \frac{1}{1+(f/f_c)^2} \tag{4b}$$

with corner frequency f_c with an exponential attenuation term described by

$$A_{att}(f) = \exp(-\pi f t^*) \tag{4c}$$

where t^* describes the energy loss at high frequencies due to attenuation. Assuming that the corner frequency is related to the stress drop, $f_c = 0.49\ v_s(\Delta\sigma/M_0)^{1/3}$, a shear-wave velocity of v_s = 3.5 km/s in the source region, and a stress drop of $\Delta\sigma$ = 1.0 MPa, the predicted corner frequency of the source-time function is above 1 Hz and therefore the observed spectrum between 0.1 and 1 Hz is dominated by attenuation effects. We therefore fix f_c at a value of 1 Hz, so that A_0 and t^* can be inferred by linear inversion. For the high-frequency events, in contrast, we invert for all three parameters (A_0, t^*, and f_c). t^* ranges from 0.6 - 4.3 s for the observed low-frequency and from 0.05 - 0.5 s for the observed high-frequency events (see Table S1 in Electronic Supplements). Detailed subsurface structural models below the InSight lander are currently being developed (e.g. Lognonné *et al.*, 2020) and will help to fine-tune these parameters in the future (see Conclusions & Outlook).

Spectral Magnitude $M^{Ma}_{W,spec,LF}$ for Low-Frequency Events

With the current interpretation that seismic waves of marsquakes in the low-frequency event family have travelled through the Martian lithosphere and mantle (see Introduction; Figure 1), we assume a volumetric seismic wave propagation for these events. By the conservation of energy, standard geometrical spreading of seismic wave amplitudes predicts that the energy in a unit area of the growing wavefront decreases as Δ^2. Body-wave amplitudes hence decay with Δ^{-1}, so we expect $\log_{10}(A_0)$ to decrease by about one unit per unit change in $\log_{10}(\Delta)$, corresponding to $a_i \approx 1.0$ (see equation 2c). Therefore, we model the decay of seismic wave amplitudes with distance for the low-frequency events equation (3a) as $a_i = (1.0 \pm 0.1)$, assuming an uncertainty of 0.1 due to leaking energy and effects of the velocity structure on geometrical spreading.

Formatted: English (United States)

In order to determine the constant c_i in equation (3a) for the low-frequency events, we model a set of several hundreds of synthetic marsquakes at $\Delta = 5^o - 150^o$ distance and down to 50 km depth for different M_0 and source mechanisms using Instaseis (van Driel *et al.*, 2015; Ceylan *et al.*, 2017) for a set of representative Mars models described in Clinton *et al.* (2017) for the time-

window before surface-wave arrival. The same set of models and seismic propagation code was used in our original pre-launch magnitude paper (Böse *et al.*, 2018). From these simulations we determine c_i = (12.6 ± 0.5), and thus we obtain for the spectral magnitude for low-frequency events (*LF*, *BB*)

$$M_{W,\mathrm{spec},LF}^{\mathrm{Ma}} = \frac{2}{3}\left(log_{10}(A_0) + (1.0 \pm 0.1)\, log_{10}(\Delta) + (12.6 \pm 0.5)\right) \tag{5a}$$

The coefficients in equation (5a) differ from those in Böse *et al.* (2018), since here a_i has been set to 1.0.

The spectral fitting procedure to determine A_0 (equation (4a)) and thus $M_{W,\mathrm{spec},LF}^{\mathrm{Ma}}$ (equation (5a)) is affected by uncertainties, which can be used to estimate magnitude errors $\sigma^2_{M_{W,\mathrm{spec},LF}^{\mathrm{Ma}}}$. It follows from error propagation

$$\begin{aligned}\sigma_M^2 = \sigma^2_{M_{W,\mathrm{spec},LF}^{\mathrm{Ma}}} = \left(\frac{2}{3}\right)^2 \Bigg[& \left|\frac{\partial M_{W,\mathrm{spec},LF}^{\mathrm{Ma}}}{\partial log_{10}(A_0)}\right|^2 \sigma^2_{log_{10}(A_0)} \\ & + log_{10}(\Delta)^2 \left|\frac{\partial M_{W,\mathrm{spec},LF}^{\mathrm{Ma}}}{\partial a_i}\right|^2 \sigma^2_{a_i} + {a_i}^2 \left|\frac{\partial M_{W,\mathrm{spec},LF}^{\mathrm{Ma}}}{\partial log_{10}(\Delta)}\right|^2 \sigma^2_{log_{10}(\Delta)} \\ & + \left|\frac{\partial M_{W,\mathrm{spec},LF}^{\mathrm{Ma}}}{\partial c_i}\right|^2 \sigma^2_{c_i} \Bigg] \\ = \frac{4}{9}\left(\sigma^2_{log_{10}(A_0)} + \right. & \left. 0.1\, log_{10}(\Delta)^2 + \sigma^2_{log_{10}(\Delta)} + 0.3\right) \\ = 0.44\, \sigma^2_{log_{10}(A_0)} + & \ 0.044\, log_{10}(\Delta)^2 + 0.44\, \sigma^2_{log_{10}(\Delta)} + 0.13 \end{aligned} \tag{5b}$$

We determine $\sigma_{log_{10}(A_0)}$ from the uncertainty (standard deviation) in spectral fitting for each low-frequency event individually. The second term, $0.044\, log_{10}(\Delta)^2$, suggests a distance-dependent error, ranging between 0.074 at $\Delta = 20^o$ and 0.17 at $\Delta = 90^o$ and that is 0.1 at $\Delta = 32^o$. $\sigma_{log_{10}(\Delta)}$ is more difficult to determine. We use distance uncertainties as provided in the InSight catalog v.5 whenever available. For events without uncertainty estimates we assume a distance error of 25% (see Discussion). The resulting magnitude uncertainties are provided in Table S1.

Spectral Magnitude $M^{\mathrm{Ma}}_{W,\mathrm{spec},HF}$ for High-Frequency Events

With the current interpretation that seismic waves of high-frequency events are guided waves travelling in the crust or in a shallow layer (see Introduction; Figure 1), we assume a surface-wave propagation for these events. The attenuation of surface-waves is generally more complex than that of body-waves. Based on values determined by Evernden *et al.* (1971), Basham (1971), and Nuttli (1973) for short-period Lg and Rg phases on Earth (see also Bormann *et al.*, 2013), we set in equation (3a) $a_i = (0.8 \pm 0.1)$ for the high-frequency events. Assuming that the spectral amplitudes at close distance to the seismic source (here: at $\Delta = 1^{o}$) are similar for both low- and high-frequency events, we determine from equation (5a) $c_i = 12.8$, and thus obtain for the spectral magnitudes for high-frequency events (*HF* and *VF*)

$$M^{\mathrm{Ma}}_{W,\mathrm{spec},HF} = \frac{2}{3}\,(log_{10}(A_0) + (0.8 \pm 0.1)\,log_{10}(\Delta) + 12.8) \qquad (5c)$$

For simplicity, we set here $\sigma_{M^{\mathrm{Ma}}_{w,\mathrm{spec},HF}} = 0.2$ for all high-frequency events, pointing out, however, that the true uncertainties, in particular considering the uncertainty in the distance estimate, could be much larger.

Calibration of Body-wave Magnitudes $m^{\mathrm{Ma}}_{\mathrm{b}}$ and $m^{\mathrm{Ma}}_{\mathrm{b}S}$ Relative to $M^{\mathrm{Ma}}_{W,\mathrm{spec}}$

In the next step, we calibrate P- and S-body-wave magnitudes, $m^{\mathrm{Ma}}_{\mathrm{b}}$ and $m^{\mathrm{Ma}}_{\mathrm{b}S}$. These magnitudes can be determined for low-frequency events (*LF*, *BB*), excluding for $m^{\mathrm{Ma}}_{\mathrm{b}S}$ the events S0325a, S0357a, S0183a, and S0205a that fall into the low (S-wave) amplitude-zone (Giardini *et al.*, 2020) (Table 1 & Figure 3). We compute $m^{\mathrm{Ma}}_{\mathrm{b}}$ and $m^{\mathrm{Ma}}_{\mathrm{b}S}$ from the peak displacement amplitudes A_P and A_S, which we determine from the integrated and filtered velocity waveforms (applying a 6$^{\mathrm{th}}$ order causal Butterworth bandpass with corner frequencies of 0.167 Hz and 0.5 Hz) in the time window of the compression- or shear-wave arrivals, respectively (Figure 2b). We use the vertical component of

the seismograms to compute A_P and the maximum of the two horizontal components to compute A_S.

From the SNR-weighted amplitude regression of A_P and A_S with $M^{\mathrm{Ma}}_{W,\mathrm{spec},LF}$, we find for the P-wave magnitudes

$$m_{\mathrm{b}}^{\mathrm{Ma}} = log_{10}(A_P) + 0.73\ log_{10}(\Delta) + 11.8 \quad (6)$$

and for S-wave magnitudes

$$m_{\mathrm{b}S}^{\mathrm{Ma}} = log_{10}(A_S) + 1.06\ log_{10}(\Delta) + 10.9 \quad (7)$$

The MQS assigns SNRs to each (time-domain) picked amplitude (Clinton *et al.*, 2020). Only the low-frequency event family (*LF* and *BB*) have significant energy between 0.2 and 0.5 Hz, so $m_{\mathrm{b}}^{\mathrm{Ma}}$ and $m_{\mathrm{b}S}^{\mathrm{Ma}}$ can be determined only for these events (Table 1). According to the MQS v.5 event catalog < 20 % of these events have a SNR of < 2.0 in the 0.2 - 0.5 Hz frequency band. These are mostly quality 'C' and 'D' events and their body-wave magnitudes are thus considered less certain.

Calibration of 2.4Hz Magnitude $M_{2.4}^{\mathrm{Ma}}$ Relative to $M_{W,\mathrm{spec}}^{\mathrm{Ma}}$

Finally, we calibrate the 2.4Hz magnitude, $M_{2.4}^{\mathrm{Ma}}$, which can be computed for all high-frequency events (*HF*, *VF*, *2.4Hz*) in the InSight v.5 catalog (Table 1). We assume a constant, magnitude-independent amplification of the 2.4 Hz resonance. We calibrate the resulting magnitudes to scale with $M_{W,\mathrm{spec}}^{\mathrm{Ma}}$ for all high-frequency events that have additional measurements of A_0 (*HF* and *8 VF* events: S0128a, S0264e, S0334a, S0376a, S0387a, S0421a, S0424c & S0475a, but no *2.4Hz*, see Table 1).

We define and calibrate the $M_{2.4}^{\mathrm{Ma}}$ in two ways: $M_{2.4,\mathrm{pick}}^{\mathrm{Ma}}$ is calculated from the time domain amplitude $A_{2.4,\mathrm{pick}}$; $M_{2.4,\mathrm{spec}}^{\mathrm{Ma}}$ is calculated from the spectral amplitude $A_{2.4,\mathrm{spec}}$. The first is computed from the peak amplitude on the vertical component in the 2-3 Hz bandpass-filtered (6th order Butterworth bandpass with corner frequencies of 2.2 Hz and 2.8 Hz) velocity waveform; the second from fitting a Lorentz curve to the displacement spectra (computed as described in the spectral magnitude section) between 2 and 3 Hz (Figure 2a).

From SNR-weighted amplitude regression of $A_{2.4,\mathrm{pick}}$ and $A_{2.4,\mathrm{spec}}$ with $M_{W,\mathrm{spec},HF}^{\mathrm{Ma}}$, we find

$$M_{2.4,\mathrm{pick}}^{\mathrm{Ma}} = log_{10}(A_{2.4,\mathrm{pick}}) + 1.0\, log_{10}(\Delta) + 10.8 \quad (8a)$$

and

$$M_{2.4,\mathrm{spec}}^{\mathrm{Ma}} = log_{10}(A_{2.4,\mathrm{spec}}) + 1.0\, log_{10}(\Delta) + 11.0 \quad (8b)$$

RESULTS

We use the event distances from the InSight MQS catalog v.5 (until 2020/10/12) and amplitudes at different frequencies (as defined above) determined by MQS (Clinton *et al.*, 2020) to determine magnitudes and uncertainties using the equations described above. Table S1 (Electronic Supplement) summarizes all parameters and resulting magnitudes.

Overall, we achieve a very good agreement across the magnitude scales with standard deviations of σ = 0.3 for $m_{\mathrm{b}}^{\mathrm{Ma}}$, $\mathrm{m}_{\mathrm{b}S}^{\mathrm{Ma}}$, and of $\sigma = 0.2$ for $M_{2.4,\mathrm{pick}}^{\mathrm{Ma}}$ and $M_{2.4,\mathrm{spec}}^{\mathrm{Ma}}$ with regards to the spectral magnitude, $M_{W,\mathrm{spec}}^{\mathrm{Ma}}$, which we used as a calibration reference (Figure 4). There is basically no difference between the sub-categories of the low- and high-frequency event families. The time domain and spectral domain resonance magnitudes, $M_{2.4,\mathrm{pick}}^{\mathrm{Ma}}$ and $M_{2.4,\mathrm{spec}}^{\mathrm{Ma}}$, are very similar, while $M_{2.4,\mathrm{spec}}^{\mathrm{Ma}}$ achieves a slightly better fit with $M_{W,\mathrm{spec}}^{\mathrm{Ma}}$. We conclude that the two spectral magnitudes, $M_{W,\mathrm{spec}}^{\mathrm{Ma}}$ and $M_{2.4,\mathrm{spec}}^{\mathrm{Ma}}$, are most robust and we thus set the preferred (moment) magnitude to

$M_W^{\mathrm{Ma}} = M_{W,\mathrm{spec},LF}^{\mathrm{Ma}}$ for *LF* and *BB* events, to $M_W^{\mathrm{Ma}} = M_{W,\mathrm{spec},HF}^{\mathrm{Ma}}$ for *HF* events, and to $M_W^{\mathrm{Ma}} = M_{2.4,\mathrm{spec}}^{\mathrm{Ma}}$ for *VF* and *2.4Hz* resonance events. The picking of peak amplitudes in the frequency domain is more stable, since a much longer time-window (5 - 30 minutes) is considered (Figure 2).

Adopting the newly calibrated scales (Table 2), we determine the magnitudes of the events in the InSight MQS catalog v.5 as $1.1 \leq M_W^{\mathrm{Ma}}(\sim M_W) \leq 3.7$ (Table S1). More specifically, we find $2.7 \leq M_W^{\mathrm{Ma}} \leq 3.7$ for the 20 *LF* events, $2.7 \leq M_W^{\mathrm{Ma}} \leq 3.5$ for the 9 *BB* events, $1.7 \leq M_W^{\mathrm{Ma}} \leq 2.6$ for the 50 *HF* events, $1.1 \leq M_W^{\mathrm{Ma}} \leq 2.9$ for the 21 *VF* events, and $1.3 \leq M_W^{\mathrm{Ma}} \leq 3.0$ for the 179 *2.4Hz* events. From equation (5b) we estimate the magnitude uncertainties for the low-frequency (*LF*, *BB*) events to range between $\sigma_M = 0.2$ and $\sigma_M = 0.5$ (Table S1). As stated before, because of the currently unclear interpretation of high-frequency events, including their distances (Giardini *et al.*, 2020; van Driel *et al.*, 2021), we simply set $\sigma_M = 0.2$, even though the true uncertainties could be much larger. Magnitude estimates for high-frequency events given in this article primarily serve for a relative comparison of these events with each other (see Discussion).

Figure 5 shows the distribution of all events as a function of epicentral distance. The four largest events are all low-frequency events: S0325a (M_W^{Ma}3.7, Δ = 38°, quality 'B'), S0167a (M_W^{Ma}3.7, Δ = 95°, quality 'C'), S0173a (M_W^{Ma}3.7, Δ = 28°, quality 'A'), and S0235b (M_W^{Ma}3.5, Δ = 27°, quality 'A'). Note that the distance estimate for S0167a is very uncertain, since it was derived from waveform envelope similarity (see Giardini *et al.*, 2020 for details). The large uncertainty in distance for S0167a is also reflected in inconsistent magnitude estimates across different scales ($m_{\mathrm{bS}}^{\mathrm{Ma}}$3.3 and $M_{W,\mathrm{spec}}^{\mathrm{Ma}}$3.7, see Table S1).

DISCUSSION

In this article, we recalibrated magnitude relations for Mars from InSight data using a seismicity catalog of a full Martian year, corresponding to nearly two Earth years. Pre-landing seismicity estimates expected larger marsquakes that more closely resembled teleseismic events we observe on Earth. Hence, our pre-landing magnitude study assumed larger events, with surface-waves and

energy at long periods (Böse *et al.*, 2018). An additional crucial difference from our pre-landing study is that the available data has included the routine collection of continuous high-sampled rate data (first 10 sps, then 20 sps) throughout the mission, instead of the 2 sps planned beforehand. This means higher frequency data than anticipated could be used. The high-frequency event class had not been expected at all and therefore required completely novel magnitude scales, as presented in this article.

(Single-station) magnitude computations are affected by assumptions made to model the seismic wave propagation from the source to the receiver. These models predict both the decay of seismic wave amplitudes and the observation of different phase arrivals at different distances, and they also impact the distance estimates relative to the receiver (Khan *et al.*, 2016). Despite collecting an exceptional seismic event dataset during the first year of the InSight mission (InSight Mars SEIS Data Service, 2019), our knowledge of Mars interior structure is still limited, which leads to unavoidable uncertainties in magnitude estimates.

Model assumptions have a strong impact on magnitude estimates as shown for the Moon. Nakamura *et al.* (1976) studied the distant-dependent decay of S-wave amplitudes on the Moon generated by artificial and meteoroid impacts as well as shallow moonquakes observed at the Apollo seismic network stations. The authors assigned lunar magnitudes to these events, estimated to be approximately 1.0 less than the Richter magnitude for the same amplitude. Goins *et al.* (1981) developed equations to estimate source parameters of shallow and deep moonquakes (seismic moment, seismic energy release, stress drop, and body-wave magnitude), from seismograms and displacement spectra that account for the effects of instrument bandwidth, variations in corner frequency, and the effects of intense scattering on the Moon. They determined the stress drops and body-wave magnitudes of the largest shallow moonquakes as 40 MPa, and ~ 5.0, respectively. Following the same method with some improvements and corrections, Oberst (1987) obtained remarkably different results with stress drops of > 100 MPa and body-wave magnitudes of > 5.5.

In our current understanding (Giardini *et al.*, 2020; van Driel *et al.*, 2021) the seismic waveforms of events in the low-frequency (*LF*, *BB*) and high-frequency (*HF, VF, 2.4Hz*) event families are dominated by mantle and crustal guided waves, respectively (Figures 1 and 2). Following this interpretation, we constrained the magnitude scales in this article, assuming a volumetric seismic wave propagation for the low-frequency and a surface propagation for the high-frequency events.

We determined the constant in equation (5a) from seismic waveform modeling through a set of representative Mars models discussed in Clinton *et al.* (2017). From equations (2b) and (2c) and $\Omega_0 \approx A_0\sqrt{N\Delta t}$, where N is the number of data samples before zero-padding in the time windows and Δt the sampling interval of the displacement time series used for the PSD computation, we would theoretically expect for S-waves that

$$c_i = log_{10}(\sqrt{N\Delta t}) + a_i\, log_{10}\left(\frac{\pi}{180}R_{Ma}\right) + log_{10}\frac{4\pi\rho {v_s}^3}{R_S^{\theta\phi} S_f} - 9.1 \qquad (9)$$

With N = 512, Δt = 0.05 s, $a_i = 1.0$, density $\rho = 3{,}500\ kg/m^3$, $v_s = (3{,}500 \pm 500)\ m/s$, average (S-wave) radiation pattern of $R_S^{\theta\phi} = 0.55$, free-surface amplification S_f = 2.0 (Boore & Boatwright, 1984), and radius of Mars R_{Ma} = 3'385 km, we obtain c_i = 0.7 + 4.8 + (15.2 ± 0.2) - 9.1 = (11.6 ± 0.2). The discrepancy between our modelled ($c_i = 12.6$) and theoretical value ($c_i = 11.6 \pm 0.2$) suggests that the theoretical approximation in equation (2b) is likely too simple for our purpose, since we are not looking at a single seismic ray from the source through a full space, but at a time window that contains both surface reflections and interfering rays. In fact, at the epicentral distances of the observed marsquakes, the seismograms can no longer be regarded as the deterministic signal that is assumed by the theory underlying equation (2b), but must be treated as transient stochastic time series with variable amplitudes and undetermined duration. Additional simulations based on the convolution of a synthetic source-time function of known seismic moment with a transient white-noise time series multiplied with a tapering function that decays exponentially with time show that the spectral analysis over a more or less arbitrary length of the S-wave coda tends to underestimate the true seismic moment. Thus, at least part of the difference between the theoretically expected value of c_i and the value of c_i derived from the

calibration procedure based on synthetic seismograms, implemented in the present study, compensates for this methodological bias.

Despite the apparent disagreement with the theoretically expected c_i coefficient, the adequacy of our magnitude scales is supported two-fold: (1) In an independent study, Brinkman *et al.* (2020) determined the magnitudes of the S0235b, S0173a, and S0183a events from moment tensor inversion as M_W3.1, M_W3.0, and M_W3.3, respectively, which is close to our values ($M_W^{\mathrm{Ma}}3.5 \pm 0.3$, $M_W^{\mathrm{Ma}}3.7 \pm 0.4$, and $M_W^{\mathrm{Ma}}3.1 \pm 0.4$ respectively; see Table S1). The remaining discrepancy can be explained, since for S0235b and S0173a, the InSight station is located close to a maximum of the S-wave radiation pattern (as estimated from the amplitude ratios of P- and S-waves on different components), resulting in an overestimation of magnitude when not inverting for the moment tensor. (2) Figure 6 compares our $m_{\mathrm{b}}^{\mathrm{Ma}}$ and $m_{\mathrm{b}S}^{\mathrm{Ma}}$ estimates from A_P and A_S for the low-frequency (*LF*, *BB*) events in the InSight catalog with the medium-period body-wave broadband magnitude, mB, proposed by Gutenberg (1945a,b) for Earth. Although developed for teleseismic P- and S-waves at 2 - 20 s period on Earth (Bormann *et al.*, 2013), we are applying the mB relations here to Mars for A_P and A_S at 2 - 6 s period. Simplifying the lookup table in Gutenberg and Richter (1956) for a source depth of 15 km and two distance intervals, we obtain

$$mB_P = log_{10}(A_P) + 12.9 \text{ for } \Delta \leq 70^o \quad (10a)$$

$$mB_P = log_{10}(A_P) + 13.2 \text{ for } \Delta > 70^o \quad (10b)$$

$$mB_S = log_{10}(A_S) + 12.6 \text{ for } \Delta \leq 70^o \quad (10c)$$

$$mB_S = log_{10}(A_S) + 13.0 \text{ for } \Delta > 70^o \quad (10d)$$

The good agreement of $m_{\mathrm{b}}^{\mathrm{Ma}}$ and $m_{\mathrm{b}S}^{\mathrm{Ma}}$ with mB_P and mB_S in Figure 6 suggests that the attenuation of body-waves at long periods and teleseismic distances on Mars and Earth are similar. While we could potentially consider applying earthquake magnitude scales, such as mB, to Mars, it needs to be pointed out again that due to the noise condition on Mars, time-domain amplitudes A_P and A_S could so far be determined only for a small subset of marsquakes. For the majority of seismic events we have only measurements of spectral amplitudes (A_0, $A_{2.4,\mathrm{spec}}$) for which no

comparable magnitude scales on Earth exist. On the other hand, the good agreement of mars- and earthquake magnitude scales in Figure 6 indicates that both the absolute calibration of $M_{W,\mathrm{spec}}^{\mathrm{Ma}}$ and the relative calibration of (at least) of $m_{\mathrm{b}}^{\mathrm{Ma}}$ and $m_{\mathrm{b}S}^{\mathrm{Ma}}$ achieve reasonable magnitude estimates.

All marsquake signals identified by MQS so far have durations of 5 to 30 minutes. This is significantly longer compared to what we would expect on Earth for the same magnitude range (M < 4), even though the comparison is difficult since such small events are usually not observed in distances of > 1500 km. We attribute these long durations mainly to the strong scattering of seismic energy on Mars (e.g., Lognonné *et al.*, 2020). On Earth, the signal length has been used to compute duration (or coda) magnitudes for strong historical and local earthquakes (Bormann *et al.*, 2013). On Mars, such a relationship, however, is not clearly visible, likely because scattering is the dominating effect on the signal duration, which is independent of the source magnitude.

Distances of low-frequency (*LF*, *BB*) events relative to the InSight lander in the event catalog (InSight Marsquake Service, 2021) were determined using the probabilistic approach of Böse *et al.* (2016), which accounts for both pick and model uncertainties. This approach requires at least 2 seismic phase picks. Absolute event locations in the catalog (including a backazimuth) were inferred only for events with a clear polarization of the seismic signals, which only applies to a small subset of events (Clinton *et al.*, 2020). As discussed in Böse *et al.* (2018), even large distance uncertainties on the order of 25% and depth errors of 20 km (L1 InSight mission requirements; Banerdt *et al.*, 2013) translate into magnitude errors of only ± 0.2 units, which is smaller than the magnitude uncertainties (± 0.5 units) that can generally be expected with a single-station approach and that are related to the variability in the focal mechanisms and uncertainties in the interior model.

A number of low-frequency events without clear emergent phase arrivals in the InSight catalog were located based on the similarity of waveform envelopes and theoretical travel-time curves using locatable events with clear phases as a reference (Giardini *et al.*, 2020). Estimating the distance (and thus magnitude) uncertainties for these events is difficult. They might be quite large, in particular for events at large distances. Phase identification for these events is ambiguous, some

of them have extremely weak P- and S-wave signals (Giardini *et al.*, 2020). For instance, it is possible that A_P (and potentially A_S) for the most distant marsquake (S0167a) at 95° distance was measured in a different phase than for the closer events, or that the event is even beyond the core shadow and we observe a SS/SSS wave train. This would also explain the different shape of the waveform envelopes as observed in Giardini *et al.* (2020). For this reason, we consider the current magnitude estimates for S0167a and other events in this distance range to be rather uncertain. Further research is needed to better understand the seismic wave propagation through Mars, which will lead to a better phase assignment and enhanced distance and thus magnitude estimates in the future.

Locating the (crustal) high-frequency (*HF*, *VF*, *2.4Hz*) events requires another approach. In the InSight catalog distances of these events were inferred from P_g-S_g travel-times using a very simple model with constant velocities of $v_p = 4$ km/s and $v_S = v_P/\sqrt{3}$ (= 2.3 km/s) (van Driel *et al.*, 2021). With this model, high-frequency events are located at distances between 3° and 40°, with the bulk between 25 and 30°, while low-frequency events are located at 20° - 95° distance (Figure 5). Assuming lower (e.g. $v_p = 2.6$ km/s and $v_S = 1.5$ km/s) or higher (e.g. $v_p = 5.2$ km/s and $v_S = 3.0$ km/s) velocities, the distances of the high-frequency events would change by approximately 10° (1° on Mars corresponds to 59.2 km). Using equation (6b), this translates again into magnitude uncertainties of ± 0.2 units, similarly to the expected uncertainties for low-frequency events, and again smaller compared to what can generally be expected with a single station approach (± 0.5 units). Because of the currently unclear interpretation of events in the high-frequency family, including large uncertainties in their distances, our magnitude estimates for these events serve primarily to enable a relative comparison of these events with each other.

Models of the subsurface structure of Mars below the InSight lander start emerging. For example, the receiver function analysis of Lognonné *et al.* (2020) suggests a 10 km low-velocity layer, which might generate some type of site effect. The 2.4 Hz resonance is probably caused by even shallower layers, but these are most likely not the ones in which the guided waves of the high-frequency events propagate (van Driel *et al.*, 2021). Nevertheless, the propagation velocity of the guided

waves could significantly differ from those we assumed at the source, resulting in a systematic bias in the moment estimation. Incorporating site effects as predicted from this and other models, which are currently being developed, could help to fine-tune magnitude estimates on Mars in the future.

CONCLUSIONS & OUTLOOK

In this article, we revised the magnitude relations in Böse *et al.* (2018) to account for the seismic and noise characteristics observed on Mars during the first Martian year of the InSight mission. In light of these observations, we updated the scaling relations for the spectral and body-wave magnitudes, $M_{W,\mathrm{spec}}^{\mathrm{Ma}}$, $m_{\mathrm{b}}^{\mathrm{Ma}}$ and $m_{\mathrm{b}S}^{\mathrm{Ma}}$, and introduced a new magnitude scale, $M_{2.4}^{\mathrm{Ma}}$, for high-frequency events. The new scales are summarized in Table 2 of this article. We recommend setting the preferred magnitude to $M_W^{\mathrm{Ma}} = M_{W,\mathrm{spec},LF}^{\mathrm{Ma}}$ for *LF* and *BB* events, to $M_W^{\mathrm{Ma}} = M_{W,\mathrm{spec},HF}^{\mathrm{Ma}}$ for *HF* events, and to $M_W^{\mathrm{Ma}} = M_{2.4,\mathrm{spec}}^{\mathrm{Ma}}$ for *VF* and *2.4Hz* resonance events. We used the new magnitude scales to determine that the magnitudes of the events in the current InSight catalog v.5 range between 1.1 and 3.7. We estimate that magnitude uncertainties are on the order of $\pm$ 0.5 magnitude units, which is mainly due to uncertainties in the focal mechanisms rather than in distances. Location uncertainties of some events in the InSight catalog, however, might be quite large, in particular for events at large distance with uncertain phase identification. Estimating the magnitude uncertainties of these events is difficult, in particular because other phase arrivals might be measured than what was used for magnitude calibration. Overall, we achieve a very good agreement across all magnitude scales with regards to the spectral magnitude, $M_{W,\mathrm{spec}}^{\mathrm{Ma}}$, which is considered a measure of the moment magnitude, M_W.

Magnitude estimates of marsquakes are a key component in the characterization of the seismic activity rate of Mars (Knapmeyer *et al.*, 2019). All pre-mission Martian seismicity models are based on estimated moment rates, which require magnitudes. Hence, magnitudes are needed to determine which models are best suited for Mars. Refining interior models of Mars from InSight observations will not only help to further refine magnitude scales for marsquakes in the future,

but also to better understand the level and distribution of seismicity on the planet. Once we have a better understanding of the source and propagation, in particular of *VF* and *SF* events, new magnitudes scales for these events will be devised.

DATA & RESOURCES

The Electronic Supplement to this article contains source parameters of marsquakes as provided in the InSight catalog v.5 (until 2020/10/12) of the InSight Marsquake Service (2021), as well as time-domain and spectral amplitudes, spectral fitting parameters and magnitudes as computed in this article.

InSight Marsquake Service (2021). Mars Seismic Catalogue, InSight Mission; V5 2021-01-04. ETHZ, IPGP, JPL, ICL, MPS, Univ. Bristol. https://doi.org/10.12686/a10.

InSight Mars SEIS Data Service (2019). SEIS raw data, Insight Mission. IPGP, JPL, CNES, ETHZ, ICL, MPS, ISAE-Supaero, LPG, MFSC. https://doi.org/10.18715/SEIS.INSIGHT.XB_2016.

InSight Mars SEIS Data Service (2019). InSight SEIS Data Bundle. PDS Geosciences (GEO) Node. https://doi.org/10.17189/1517570.

Please be aware that the InSight catalog can change over time reflecting our respective understanding of Mars seismicity and its interior structure. The most recent event InSight catalog can be retrieved from https://www.iris.edu/hq/sis/insight.

ACKNOWLEDGEMENTS

We would like to thank two anonymous reviewers, Guest Editor Sharon Kedar and Editor-in-Chief Thomas Pratt for their positive feedback and comments. We acknowledge NASA, CNES, their partner agencies and institutions (UKSA, SSO, DLR, JPL, IPGP-CNRS, ETHZ, IC, MPS-MPG) and the flight operations team at JPL, SISMOC, MSDS, IRIS-DMC and PDS for providing SEED SEIS data. We acknowledge funding from (1) Swiss State Secretariat for Education, Research and Innovation (SEFRI project “MarsQuake Service-Preparatory Phase”), (2) ETH Research grant ETH-06 17-02, and (3) ETH+02 19-1: Planet MARS. The Swiss contribution in implementation of the SEIS

electronics was made possible through funding from the federal Swiss Space Office (SSO), the contractual and technical support of the ESA-PRODEX office. The French authors acknowledge the French Space Agency CNES and ANR (ANR-14-CE36-0012-02 and ANR-19-CE31-0008-08) for support in the Science analysis. This is InSight contribution #186.

REFERENCES

Aki, K., & Richards, P. G. (1980). *Quantitative seismology: Theory and methods*. San Francisco: W.H. Freeman.

Banerdt, W. B., S. Smrekar, P. Lognonné, T. Spohn, S. W. Asmar, D. Banfield, L. Boschi, U. Christensen, V. Dehant, W. Folkner, et al. (2013). InSight: A discovery mission to explore the interior of Mars, Lunar and Planetary Science Conference, Lunar and Planetary Institution. Technical Report, Vol. 44, 1915 pp.

Banerdt, W.B., S. Smrekar, P. Lognonné, D. Giardini, et al. (2020). Early Results from the InSight Mission: Surface Environment and Global Seismic Activity, *Nature Geoscience*, 13, 183–189(2020), doi: 10.1038/s41561-020-0544-y.

Basham, P. W. (1971). A New Magnitude Formula for Short Period Continental Rayleigh Waves, *Geophys. J. Int.* 23(2), 255–260, https://doi.org/10.1111/j.1365-246X.1971.tb01817.x.

Bisztricsany, E. (1958). *A new method for the determination of the magnitude of earthquake. Geofiz. Kozl.*, **7**, 69-96 (in Hungarian with English abstract).

Brune, J. N. (1970). Tectonic stress and the spectra of seismic shear waves from earthquakes, *J. Geophys. Res.*, 75(26), 4997–5009, doi:10.1029/JB075i026p04997.

Böse, M., Clinton, J. F., Ceylan, S., Euchner, F., van Driel, M., Khan, A., *et al.* (2016). A Probabilistic Framework for Single-Station Location of Seismicity on Earth and Mars. *Physics of the Earth and Planetary Interiors*, *262*, 48–65. https://doi.org/10.1016/j.pepi.2016.11.003

Böse, M., Giardini, D., Stähler, S. C., Ceylan, S., Clinton, J. F., van Driel, M., et al. (2018). Magnitude Scales for Marsquakes. *Bull. Seismol. Soc. Am. 108*(5A), 2764–2777. https://doi.org/10.1785/0120180037

Boore, D., and J. Boatwright (1984). Average body-wave radiation coefficients, *Bull. Seism. Soc. Am.*, 74, 1615-1621.

Bormann, P., S. Wendt, D. DiGiacomo (2013). Seismic sources and source parameters, In: Bormann, P. (Ed.), New Manual of Seismological Observatory Practice 2 (NMSOP2), Potsdam, Deutsches GeoForschungsZentrum GFZ, 1-259, https://doi.org/10.2312/GFZ.NMSOP-2_ch3.

Brinkman, N., S. Stähler, D. Giardini, C. Schmelzbach, A. Jacob, N. Fuji, C. Perrin, P. Lognonné, M. Böse, B. Knapmeyer-Endrun, E. Beucler, E. et al. (2020). Single-station moment tensor inversion on Mars, *J. Geophys. Res. – Planets,* 10.1002/essoar.10503341.1.

Ceylan, S., van Driel, M., Euchner, F., Khan, A., Clinton, J., Krischer, L., Böse, M., Stähler, S. and D. Giardini (2017). From initial models of seismicity, structure and noise to synthetic seismograms for Mars, *Space Science Reviews*, InSight special issue, DOI 10.1007/s11214-017-0380-6.

Ceylan, S., J. Clinton, D. Giardini, M. Böse, C. Charalambous, e*t al.* (2020). Companion guide to the Marsquake catalog from InSight, sols 0–478: Data content and non-seismic events, *Physics of the Earth and Planetary Interiors*, https://doi.org/10.1016/j.pepi.2020.106597

Charalambous, C., Stott, A. E., Pike, W. T., McClean, J. B., Warren, T., Spiga, A., et al. (2021). A Comodulation Analysis of Atmospheric Energy Injection into the Ground Motion at InSight, Mars. *Journal of Geophysical Research: Planets* 126, e2020JE006538. https://doi.org/10.1029/2020JE006538

Clinton, J. F., Giardini, D., Böse, M., Ceylan, S., van Driel, M., Euchner, F., *et al.* (2018). The Marsquake Service: Securing Daily Analysis of SEIS Data and Building the Martian Seismicity Catalogue for InSight. *Space Science Reviews*, *214*(8), 133. doi:10.1007/s11214-018-0567-5.

Clinton, J. F., D. Giardini, P. Lognonné, B. Banerdt, M. van Driel, M. Drilleau, N. Murdoch, M. Panning, R. Garcia, D. Mimoun, M. Golombek, J. Tromp, R. Weber, M. Böse, S. Ceylan, I. Daubar, B. Kenda, A. Khan, L. Perrin, and A. Spiga (2017). Preparing for InSight: an invitation to participate in a blind test for Martian seismicity, *Seismol. Res. Lett.* 88(5), 1290-1302, doi: 10.1785/0220170094.

Clinton, J.F., S. Ceylan, M. van Driel, D. Giardini, S.C. Stähler, M. Böse *et al.* (2020). The Marsquake Catalogue from InSight, Sols 0-478, *Physics of the Earth and Planetary Interiors*, https://doi.org/10.1016/j.pepi.2020.106595.

Dahmen, N. L., Clinton, J. F., Ceylan, S., van Driel, M., Giardini, D., Khan, A., et al. (2021). Super high frequency events: A new class of events recorded by the InSight seismometers on

Mars. *Journal of Geophysical Research: Planets* 126, e2020JE006599. https://doi.org/10.1029/2020JE006599

Dahmen, N., G. Zenhäusern, et al. (subm.): Resonances and Lander Modes observed by InSight on Mars (1-9∼Hz), submitted to BSSA.

Giardini, D., P. Lognonné, W. Banerdt, W. Pike, U. Christensen, S. Ceylan, J. Clinton, M. van Driel, S. Stähler, M. Böse *et al.* (2020). The Seismicity of Mars, *Nature Geoscience*, 13, 1-8, doi: 10.1038/s41561-020-0539-8.

Goins, N.R., A.M. Dainty, and M.N. Toksöz (1981). Seismic energy release of the Moon, *J. Geophys. Res.* 86: 378–388.

Gutenberg, B. (1945a). Amplitudes of P, PP, and S and magnitude of shallow earthquakes. *Bull. Seism. Soc*. Am. 35, 57-69.

Gutenberg, B. (1945b). Magnitude determination of deep-focus earthquakes. *Bull. Seism. Soc. Am.*, 35, 117-130.

Gutenberg, B., and Richter, C. F. (1956). Magnitude and energy of earthquakes, *Annali di Geofisica*, 9, 1-15.

Hanks, T.C. and H. Kanamori (1979). A Moment magnitude scale, *J. Geophys. Res.* 84 (B5), doi:10.1029/JB084iB05p02348.

InSight Mars SEIS Data Service (2019). SEIS raw data, Insight Mission. IPGP, JPL, CNES, ETHZ, ICL, MPS, ISAE-Supaero, LPG, MFSC. https://doi.org/10.18715/SEIS.INSIGHT.XB_2016.

InSight Mars SEIS Data Service (2019). InSight SEIS Data Bundle. PDS Geosciences (GEO) Node. https://doi.org/10.17189/1517570.

InSight Marsquake Service (2021). Mars Seismic Catalogue, InSight Mission; V5 2021-01-04. ETHZ, IPGP, JPL, ICL, MPS, Univ. Bristol. https://doi.org/10.12686/a10.

Kennett, B. L. N. and T. Furumura (2013). High-frequency *Po/So* guided waves in the oceanic lithosphere: I—long-distance propagation, *Geophysical Journal International* 195(3), 1862–1877, https://doi.org/10.1093/gji/ggt344.

Khan, A., van Driel, M., Böse, M., Giardini, D., Ceylan, S., Yan, J., . . . Banerdt, W. B. (2016). Single-station and single-event marsquake location and inversion for structure using synthetic Martian waveforms, *Phys. Earth Planet. Inter.* 258, 28-42. doi: https://doi.org/10.1016/j.pepi.2016.05.017.

Knapmeyer, M., B. Knapmeyer-Endrun, A.-C. Plesa, M. Böse, T. Kawamura, J.F. Clinton, M.P. Golombek, S. Kedar, S. Stähler, J. Stevanović, C. Perrin, P. Lognonné, N.A. Teanby, and R. Weber (2019). Estimation of the Seismic Moment Rate from an Incomplete Seismicity Catalog, in the Context of the InSight Mission to Mars, *Bull. Seismol. Soc. Am.*, 109 (3), 1125-1147, https://doi.org/10.1785/0120180258.

Lognonné, P., W B. Banerdt, D. Giardini, W. T. Pike, U. Christensen, and et al. (2020). First constraints on the shallow elastic and anelastic structure of Mars from InSight data, *Nature Geoscience*, 13, 213-220, doi: 10.1038/s41561-020-0536-y.

Lognonné, P., Banerdt, W. B., Giardini, D., Pike, W. T., Christensen, U., Laudet, P., et al. (2019). SEIS: Insight's Seismic Experiment for Internal Structure of Mars. *Space Science Reviews*, *215*(1), 12. https://doi.org/10.1007/s11214-018-0574-6

Mimoun, D., Murdoch, N., Lognonné, P., Hurst, K., Pike, W.T., Hurley, J., Nebut, T. & Banerdt, W.B. (2017). The Noise Model of the SEIS Seismometer of the InSight Mission to Mars, *Space Science Review*, doi: 10.1007/s11214-017-0409-x.

Nakamura, Y., Duennebier, F. K., Latham, G. V., and Dorman, H. J. (1976). Structure of the lunar mantle, *J. Geophys. Res.*, 81(26), 4818– 4824, doi:10.1029/JB081i026p04818.

Nissen-Meyer, T., van Driel, M., Stähler, S. C., Hosseini, K., Hempel, S., Auer, L., Colombi, A., & Fournier, A. (2014). AxiSEM: broadband 3-D seismic wavefields in axisymmetric media. Solid Earth, 5(1), 425–445. https://doi.org/10.5194/se-5-425-2014.

Nuttli, O. W. (1973). Seismic wave attenuation and magnitude relations for eastern North America, *J. Geophys. Res.*, 78(5), 876– 885, doi:10.1029/JB078i005p00876.

Oberst, J. (1987). Unusually high stress drop associated with shallow moonquakes, *J. Geophys. Res.* 92: 1397–1405.

van Driel, M., Ceylan, S., Clinton, J. F., Giardini, D., Horleston, A., Margerin, L., et al. (2021). High-frequency seismic events on Mars observed by InSight. *Journal of Geophysical Research: Planets*, 126, e2020JE006670. https://doi.org/10.1029/2020JE006670

van Driel, M., Krischer, L., Stähler, S. C., Hosseini, K., and T. Nissen-Meyer (2015). Instaseis: instant global seismograms based on a broadband waveform database, *Solid Earth* 6, 701-717, http://dx.doi.org/10.5194/se-6-701-2015.

Mailing Address for each Author

Maren Böse, Institute of Geophysics, Swiss Seismological Service (SED), ETH Zurich, Sonneggstr. 5, 8092 Zurich, Switzerland;mboese@sed.ethz.ch, https://orcid.org/0000-0003-4639-719X

Simon Stähler, Institute of Geophysics, ETH Zürich, Sonneggstrasse 5, 8092 Zürich, Switzerland; simon.staehler@erdw.ethz.ch, https://orcid.org/0000-0002-0783-2489

Nicholas Deichmann, Swiss Seismological Service (SED), ETH Zurich, Sonneggstr. 5, 8092 Zurich, Switzerland; deichmann@sed.ethz.ch

Domenico Giardini, Institute of Geophysics, ETH Zurich, Sonneggstr. 5, 8092 Zurich, Switzerland; domenico.giardini@erdw.ethz.ch, https://orcid.org/0000-0002-5573-7638

John Clinton, Swiss Seismological Service (SED), ETH Zurich, Sonneggstr. 5, 8092 Zurich, Switzerland; jclinton@sed.ethz.ch, https://orcid.org/0000-0001-8626-2703

Philppe Lognonné, Université de Paris, Institut de physique du globe de Paris, CNRS, F-75005 Paris, France; lognonne@ipgp.fr, https://orcid/org/0000-0002-1014-920X

Savas Ceylan, Institute of Geophysics, ETH Zurich, Sonneggstr. 5, 8092 Zurich, Switzerland; savas.ceylan@erdw.ethz.ch; https://orcid.org/0000-0002-6552-6850

Martin van Driel, Institute of Geophysics, ETH Zurich, Sonneggstr. 5, 8092 Zurich, Switzerland; vandriel@erdw.ethz.ch, https://orcid.org/0000-0002-8938-4615

Constantinos Charalambous, Department of Electrical and Electronic Engineering, Imperial College London, South Kensington Campus, London, SW7 2AZ, United Kingdom; constantinos.charalambous@imperial.ac.uk, https://orcid.org/0000-0002-9139-3895

Nikolaj Dahmen, Institute of Geophysics, ETH Zurich, Sonneggstr. 5, 8092 Zurich, Switzerland; nikolaj.dahmen@erdw.ethz.ch, https://orcid.org/0000-0002-9114-6747

Anna Horleston, School of Earth Sciences, University of Bristol, Wills Memorial Building, Queens Road, Bristol BS8 1RJ, UK; anna.horleston@bristol.ac.uk, https://orcid.org/0000-0002-6748-6522

Taichi Kawamura, Université de Paris, Institut de physique du globe de Paris, CNRS, F-75005 Paris, France; kawamura@ipgp.fr

Amir Khan, Institute of Geophysics, ETH Zurich, Sonneggstr. 5, 8092 Zurich, Switzerland; akhan@ethz.ch, https://orcid.org/0000-0003-4462-3173

Martin Knapmeyer, DLR Institute of Planetary Research, Rutherfordstr. 2, 12489 Berlin, Germany; martin.knapmeyer@dlr.de, https://orcid.org/0000-0003-0319-2514

Guénolé Orhand-Mainsant, Institut Supérieur de l'Aéronautique et de l'Espace SUPAERO, 10 Avenue Edouard Belin, 31400 Toulouse, France; guenole.orhand-mainsant@isae-supaero.fr, https://orcid.org/0000-0003-4923-5241

John-Robert Scholz, Max Planck Institute for Solar System Research, Justus-von-Liebig-Weg 3, 37077 Göttingen, Germany; scholz@mps.mpg.de, https://orcid.org/0000-0003-1404-2335

Fabian Euchner, Institute of Geophysics, ETH Zurich, Sonneggstr. 5, 8092 Zurich, Switzerland; fabian.euchner@sed.ethz.ch, https://orcid.org/0000-0001-6340-7439

W. Bruce Banerdt, Jet Propulsion Laboratory, California Institute of Technology, Pasadena, CA 91109, USA; bruce.banerdt@jpl.nasa.gov, https://orcid.org/0000-0003-3125-1542

Tables

Table 1. Number of seismic events for different event families and categories in the InSight v.5 catalog (until 2020/10/12; InSight Marsquake Service, 2021) that we use for magnitude calibration of four magnitude scales: spectral magnitude, $M_{w,\mathrm{spec}}^{\mathrm{Ma}}$, P- and S-body-wave magnitudes, $m_{\mathrm{b}}^{\mathrm{Ma}}$ and $m_{\mathrm{b}S}^{\mathrm{Ma}}$, and 2.4 Hz magnitude, $M_{2.4}^{\mathrm{Ma}}$. We only use events with distance estimates. Four events (S0183a, S205a, S0325a and S0357a, see Table S1) are excluded from the calibration of $m_{\mathrm{b}S}^{\mathrm{Ma}}$, because they fall into the low (S-wave) amplitude-zone of Mars (Giardini *et al.*, 2020). $M_{w,\mathrm{spec}}^{\mathrm{Ma}}$ is used as a calibration reference for the other scales for events with multiple amplitude measurements: it is most closely related to the moment magnitude M_W, less affected by noise, and can be determined for three out of five event categories.

Event family	**Event category**	**Number of events**	$\boldsymbol{M_{W,\mathrm{spec}}^{\mathrm{Ma}}}$ spectral domain	$\boldsymbol{m_{\mathrm{b}}^{\mathrm{Ma}}}$ time domain	$\boldsymbol{m_{\mathrm{b}S}^{\mathrm{Ma}}}$ time domain	$\boldsymbol{M_{2.4}^{\mathrm{Ma}}}$ spectral or time domain
Low-frequency	Low-frequency (*LF*)	20	20	20	16	-
	Broadband (*BB*)	9	9	9	8	-
High-frequency	High-frequency (*HF*)	50	50	-	-	50
	Very high-frequency (*VF*)	21	8	-	-	21
	2.4 Hz resonance (*2.4Hz*)	179	-	-	-	179

Table 2. Resulting magnitude scales for marsquakes. Spectral amplitudes A_0 (at 20 – 100 s) and $A_{2.4,\mathrm{spec}}$ (at 2 – 3 Hz) are in $m/\sqrt{Hz}$, time domain amplitudes A_P, A_S (both at 0.2 - 0.5 Hz) and $A_{2.4,\mathrm{pick}}$ (at 2 – 3 Hz) in m, and epicentral distance Δ in ° [degrees].

Name	Equation	Event family & categories	Calibrated Distance Range
Spectral magnitude	$M_{W,\mathrm{spec},LF}^{\mathrm{Ma}} = 2/3\big(log_{10}(A_0) + (1.0 \pm 0.1)\ log_{10}(\Delta) + (12.6 \pm 0.5)\big)$	Low-frequency (*LF*, *BB*)	$25^o \leq \Delta \leq 100^o$
Spectral magnitude	$M_{W,\mathrm{spec},HF}^{\mathrm{Ma}} = 2/3(log_{10}(A_0) + (0.8 \pm 0.1)\ log_{10}(\Delta) + 12.8)$	High-frequency (*HF, VF*)	$3^o \leq \Delta \leq 30^o$
Body-wave magnitude (P-wave)	$m_{\mathrm{b}}^{\mathrm{Ma}} = log_{10}(A_P) + 0.73\ log_{10}(\Delta) + 11.8$	Low-frequency (*LF*, *BB*)	$25^o \leq \Delta \leq 100^o$
Body-wave magnitude (S-wave)	$m_{\mathrm{bS}}^{\mathrm{Ma}} = log_{10}(A_S) + 1.06\ log_{10}(\Delta) + 10.9$	Low-frequency (*LF*, *BB*)	$25^o \leq \Delta \leq 35^o$ $60^o \leq \Delta \leq 100^o$
2.4Hz magnitude (time domain)	$M_{2.4,\mathrm{pick}}^{\mathrm{Ma}} = log_{10}(A_{2.4,\mathrm{pick}}) + 1.0\ log_{10}(\Delta) + 10.8$	High-frequency (*VF, HF, 2.4Hz*)	$3^o \leq \Delta \leq 35^o$
2.4Hz magnitude (spectral domain)	$M_{2.4,\mathrm{spec}}^{\mathrm{Ma}} = log_{10}(A_{2.4,\mathrm{spec}}) + 1.0\ log_{10}(\Delta) + 11.0$	High-frequency (VF, *HF, 2.4Hz*)	$3^o \leq \Delta \leq 35^o$

Figure Captions

Figure 1. Seismic wave propagation on Mars. The current interpretation of seismic signals on Mars is that events in the high-frequency event family (*HF*, *VF*) excite guided waves in the crust or in a shallow layer, while events in the low-frequency family (*LF*, *BB*) are located below the Moho; these mantle waves are observed at long periods due to attenuation. A low-velocity layer (LVL) could potentially explain the observed distant-dependent variation of S-wave amplitudes. Modified after Giardini *et al.* (2020).

Figure 2. Amplitude computation from marsquake spectra and waveforms. (a) Theoretical spectral shape of power spectral density (PSD) displacement spectra for events of the low-frequency (*LF*, *BB*; red) and high-frequency (*HF*, *VF*; blue) event families for various magnitudes. Black line shows typical background noise. (b) Filtered displacement waveforms (vertical component). Spectral amplitudes A_0 and $A_{2.4,\mathrm{spec}}$ in (a) are determined from the long-period plateau of the event displacement spectra and from a Lorentz curve fitted to the 2.4 Hz resonance peak, respectively. Peak displacement amplitudes A_P and A_S in (b) are determined from the filtered (2 - 6 s, top) displacement waveforms in the time window of the P- or S-wave arrivals. Note that A_S is actually picked on the horizontals, while we only show vertical components for the sake of simplicity. $A_{2.4,\mathrm{pick}}$ in (b) is determined from the peak amplitude of the 2-3 Hz filtered displacement waveform (bottom). Subplots in (c) and (d) show example spectra and waveforms (vertical components) of representative marsquakes of each event category: *LF* – low-frequency, *BB* – broadband, *HF* – high-frequency, *VF* – very high-frequency, and *2.4Hz* – 2.4Hz ambient resonance event.

Figure 3. Magnitude calibration for marsquakes. First, we calibrate the spectral magnitude $M^{\mathrm{Ma}}_{W,\mathrm{spec}}$ from synthetic waveforms and theoretical considerations (see main text). Then we calibrate the other magnitude scales (body-wave magnitudes $m^{\mathrm{Ma}}_{\mathrm{b}}$and $m^{\mathrm{Ma}}_{\mathrm{bS}}$, and 2.4 Hz magnitude $M^{\mathrm{Ma}}_{2.4}$) relative to $M^{\mathrm{Ma}}_{W,\mathrm{spec}}$ for events with multiple amplitude measurements (A_0 - spectral plateau amplitude; A_P, A_S - time domain peak P- and S-wave amplitudes at 0.2 – 0.5 Hz; $A_{2.4}$- resonance amplitude at 2 - 3 Hz in either time or spectral domain).

Figure 4. Marsquake magnitudes relative to spectral magnitude, $\mathbf{M^{Ma}_{W,spec}}$. Body-wave magnitudes (a) $m^{\mathrm{Ma}}_{\mathrm{b}}$ and (b) $m^{\mathrm{Ma}}_{\mathrm{bS}}$ for low-frequency events (*LF*, *BB*), and 2.4Hz magnitudes (c) $M^{\mathrm{Ma}}_{2.4,\mathrm{pick}}$ and (d) $M^{\mathrm{Ma}}_{2.4,\mathrm{spec}}$ for high-frequency events (*HF*) relative to spectral magnitude, $M^{\mathrm{Ma}}_{W,\mathrm{spec}}$, which has been used as a calibration reference (and considered to scale with moment magnitude, M_W). Markersize scales with event SNR. The calibration achieves good agreement across the different scales with standard deviations of σ = 0.3 for $m^{\mathrm{Ma}}_{\mathrm{b}}$, $m^{\mathrm{Ma}}_{\mathrm{bS}}$, and of $\sigma = 0.2$ for $M^{\mathrm{Ma}}_{2.4,\mathrm{pick}}$ and $M^{\mathrm{Ma}}_{2.4,\mathrm{spec}}$. The *HF* outlier in (c) is produced by S0490a .

Figure 5. Magnitude and distance distribution of marsquakes in the InSight catalog. Plot shows all low-frequency (*LF*), broadband (*BB*), high-frequency (*HF*), very high-frequency (*VF*) and 2.4Hz resonance (*2.4Hz*) events. The preferred magnitude is $M_W^{\mathrm{Ma}} = M_{W,\mathrm{spec},LF}^{\mathrm{Ma}}$ for *LF* and *BB* events, to $M_W^{\mathrm{Ma}} = M_{W,\mathrm{spec},HF}^{\mathrm{Ma}}$ for *HF* events, and to $M_W^{\mathrm{Ma}} = M_{2.4,\mathrm{spec}}^{\mathrm{Ma}}$ for *VF* and *2.4Hz* resonance events. Distances are derived from phase picks (InSight Marsquake Service, 2021), waveform envelope alignment (Giardini *et al.*, 2020), and a simple crustal model (van Driel *et al.*, 2021), respectively. Markersize scales with event SNR. Error bars show estimated magnitude and distance uncertainties. Both distances and magnitudes for the most distant events are uncertain.

Figure 6. Comparison with magnitude scales on Earth. Comparison of (a) $m_{\mathrm{b}}^{\mathrm{Ma}}$ and (b) $m_{\mathrm{b}S}^{\mathrm{Ma}}$ with the body-wave broadband magnitude, mB (Gutenberg, 1945a,b) for P- and S-waves on Earth for all *LF* and *BB* events in the InSight v.5 catalog. Although developed for teleseismic waves at 2 - 20 s period on Earth, we are applying the mB relations here to Mars for A_P and A_S at 2 - 6 s period. The good agreement of magnitudes on Mars and Earth suggests a similar attenuation of body-waves at long periods and teleseismic distances.

Figures

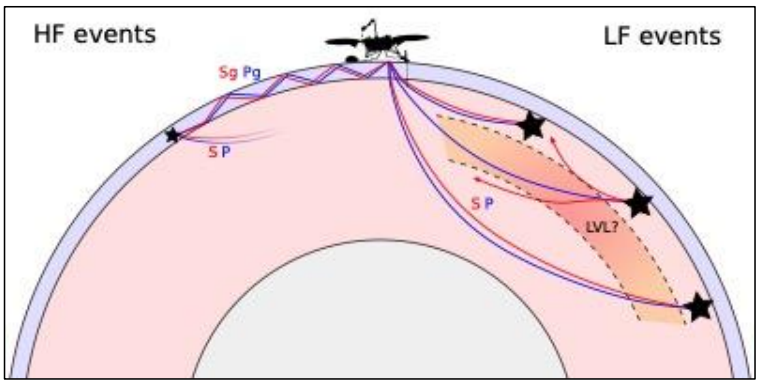

Figure 1. Seismic wave propagation on Mars. The current interpretation of seismic signals on Mars is that events in the high-frequency event family (*HF*, *VF*) excite guided waves in the crust or in a shallow layer, while events in the low-frequency family (*LF*, *BB*) are located below the Moho; these mantle waves are observed at long periods due to attenuation. A low-velocity layer (LVL) could potentially explain the observed distant-dependent variation of S-wave amplitudes. Modified after Giardini *et al.* (2020).

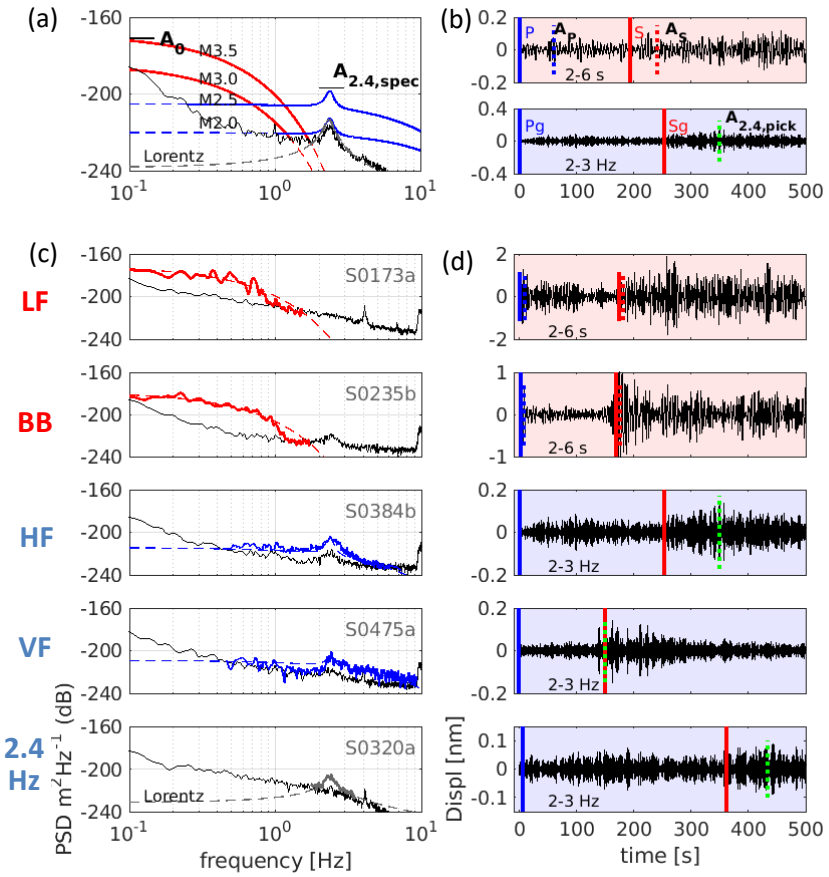

Figure 2. Amplitude computation from marsquake spectra and waveforms. (a) Theoretical spectral shape of power spectral density (PSD) displacement spectra for events of the low-frequency (*LF*, *BB*; red) and high-frequency (*HF*, *VF*; blue) event families for various magnitudes. Black line shows typical background noise. (b) Filtered displacement waveforms (vertical component). Spectral amplitudes A_0 and $A_{2.4,spec}$ in (a) are determined from the long-period plateau of the event displacement spectra and from a Lorentz curve fitted to the 2.4 Hz resonance peak, respectively. Peak displacement amplitudes A_P and A_S in (b) are determined from the filtered (2 - 6 s, top) displacement waveforms in the time window of the P- or S-wave arrivals. Note that A_S is actually picked on the horizontals, while we only show vertical components for the sake of simplicity. $A_{2.4,pick}$ in (b) is determined from the peak amplitude of the 2-3 Hz filtered displacement waveform (bottom). Subplots in (c) and (d) show example spectra and waveforms (vertical components) of representative marsquakes of each event category: *LF* – low-frequency, *BB* – broadband, *HF* – high-frequency, *VF* – very high-frequency, and *2.4Hz* – 2.4Hz ambient resonance event.

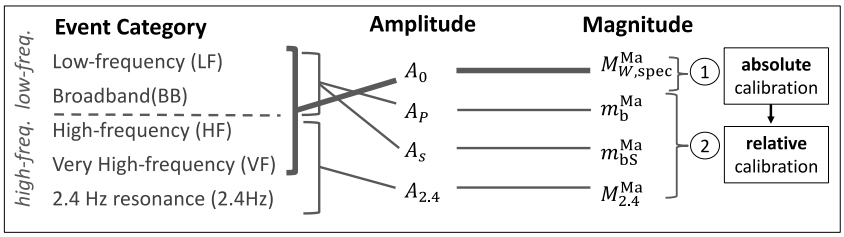

Figure 3. Magnitude calibration for marsquakes. First, we calibrate the spectral magnitude $M_{W,\mathrm{spec}}^{\mathrm{Ma}}$ from synthetic waveforms and theoretical considerations (see main text). Then we calibrate the other magnitude scales (body-wave magnitudes $m_{\mathrm{b}}^{\mathrm{Ma}}$and $m_{\mathrm{bS}}^{\mathrm{Ma}}$, and 2.4 Hz magnitude $M_{2.4}^{\mathrm{Ma}}$) relative to $M_{W,\mathrm{spec}}^{\mathrm{Ma}}$ for events with multiple amplitude measurements (A_0 - spectral plateau amplitude; A_P, A_S - time domain peak P- and S-wave amplitudes at 0.2 – 0.5 Hz; $A_{2.4}$- resonance amplitude at 2 - 3 Hz in either time or spectral domain).

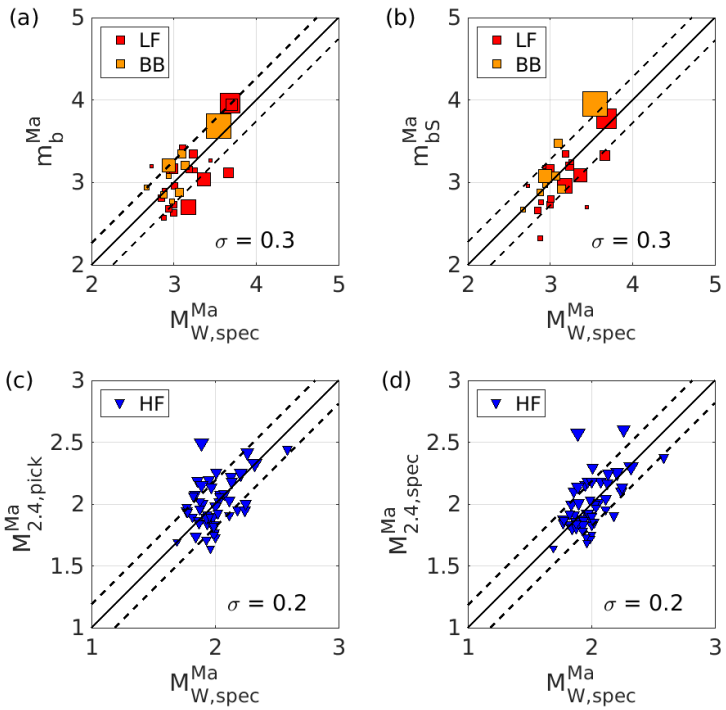

Figure 4. Marsquake magnitudes relative to spectral magnitude, $\mathbf{M^{Ma}_{W,spec}}$. Body-wave magnitudes (a) m_b^{Ma} and (b) m_{bS}^{Ma} for low-frequency events (*LF*, *BB*), and 2.4Hz magnitudes (c) $M_{2.4,pick}^{Ma}$ and (d) $M_{2.4,spec}^{Ma}$ for high-frequency events (*HF*) relative to spectral magnitude, $M_{W,spec}^{Ma}$, which has been used as a calibration reference (and considered to scale with moment magnitude, M_W). Markersize scales with event SNR. The calibration achieves good agreement across the different scales with standard deviations of σ = 0.3 for m_b^{Ma}, m_{bS}^{Ma}, and of σ = 0.2 for $M_{2.4,pick}^{Ma}$ and $M_{2.4,spec}^{Ma}$. The *HF* outlier in (c) is produced by S0490a.

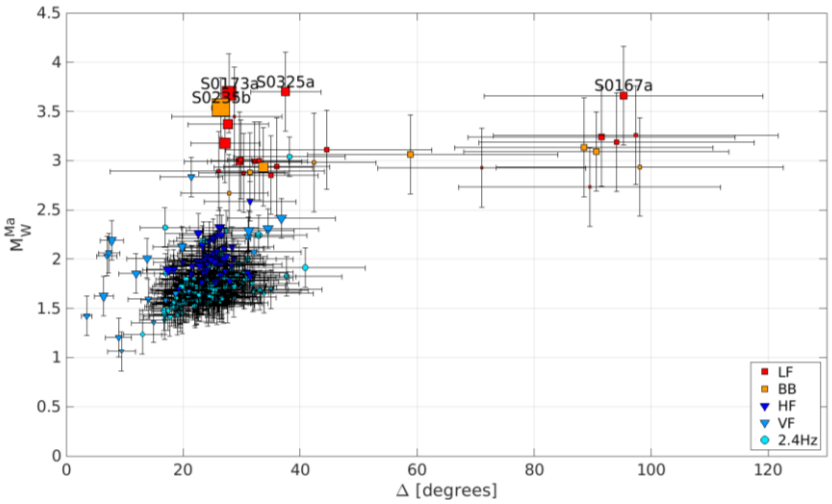

Figure 5. Magnitude and distance distribution of marsquakes in the InSight catalog. Plot shows all low-frequency (*LF*), broadband (*BB*), high-frequency (*HF*), very high-frequency (*VF*) and 2.4Hz resonance (*2.4Hz*) events. The preferred magnitude is $M_W^{\mathrm{Ma}} = M_{W,\mathrm{spec},LF}^{\mathrm{Ma}}$ for *LF* and *BB* events, to $M_W^{\mathrm{Ma}} = M_{W,\mathrm{spec},HF}^{\mathrm{Ma}}$ for *HF* events, and to $M_W^{\mathrm{Ma}} = M_{2.4,\mathrm{spec}}^{\mathrm{Ma}}$ for *VF* and *2.4Hz* resonance events. Distances are derived from phase picks (InSight Marsquake Service, 2021), waveform envelope alignment (Giardini *et al.*, 2020), and a simple crustal model (van Driel *et al.*, 2021), respectively. Markersize scales with event SNR. Error bars show estimated magnitude and distance uncertainties. Both distances and magnitudes for the most distant events are uncertain.

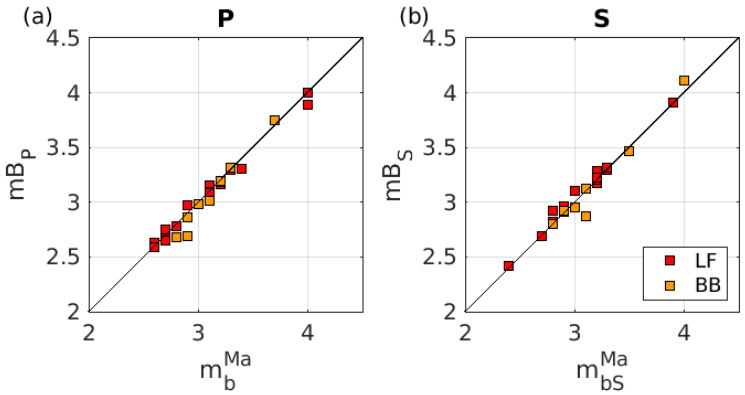

Figure 6. Comparison with magnitude scales on Earth. Comparison of (a) m_b^{Ma} and (b) m_{bS}^{Ma} with the body-wave broadband magnitude, mB (Gutenberg, 1945a,b) for P- and S-waves on Earth for all *LF* and *BB* events in the InSight v.5 catalog. Although developed for teleseismic waves at 2 - 20 s period on Earth, we are applying the mB relations here to Mars for A_P and A_S at 2 - 6 s period. The good agreement of magnitudes on Mars and Earth suggests a similar attenuation of body-waves at long periods and teleseismic distances.